nature materials

Article

https://doi.org/10.1038/s41563-025-02249-z

Hybrid epoxy–acrylate resins for wavelength-selective multimaterial 3D printing

Received: 8 April 2024

Accepted: 22 April 2025

Published online: 30 June 2025

Check for updates

Ji-Won Kim[1,4], Marshall J. Allen[1,2,4], Elizabeth A. Recker[2], Lynn M. Stevens[1], Henry L. Cater[1], Ain Uddin[1], Ang Gao[3], Wyatt Eckstrom[3], Anthony J. Arrowood[2], Gabriel E. Sanoja[2], Michael A. Cullinan[3], Benny D. Freeman[2] & Zachariah A. Page[1,2]

Structures in nature combine hard and soft materials in precise three-dimensional (3D) arrangements, imbuing bulk properties and functionalities that remain elusive to mimic synthetically. However, the potential for biomimetic analogues to seamlessly interface hard materials with soft interfaces has driven the demand for innovative chemistries and manufacturing approaches. Here, we report a liquid resin for rapid, high-resolution digital light processing (DLP) 3D printing of multimaterial objects with an unprecedented combination of strength, elasticity and resistance to ageing. A covalently bound hybrid epoxy–acrylate monomer precludes plasticization of soft domains, while a wavelength-selective photosensitizer accelerates cationic curing of hard domains. Using dual projection for multicolour DLP 3D printing, bioinspired metamaterial structures are fabricated, including hard springs embedded in a soft cylinder to adjust compressive behaviour and a detailed knee joint featuring 'bones' and 'ligaments' for smooth motion. Finally, a proof-of-concept device demonstrates selective stretching for electronics.

Objects with uniform compositions (that is, monoliths) are nearly absent from biological structures[1,2]. Instead, nature brings together multiple materials having disparate mechanical properties (for example, hard and soft) in a specific spatial arrangement. This evolved combination of composition and structure leads to unparalleled precision in functionality that cannot be achieved with a single material, sparking a flurry of research efforts to create scalable synthetic analogues using advanced manufacturing processes that offer high-dimensional accuracy, resolution and build speeds (for example, 3D printing)[3–5]. Several contemporary hurdles have prevented this realization, from slow production rates to unstable or mechanically weak products. Collectively achieving the following benchmarks in layer-based 3D printing would represent a major step towards overcoming these barriers: (1) *z*-build speed of >0.1 mm min^{-1} (<60 s per 100-µm layer), (2) lack of small molecules in final parts (limited sol fraction), (3) >1,000-fold stiffness difference (ΔE) between hard and soft materials, (4) hard-material strength of >50 MPa, (5) soft-material deformation of >100% strain, (6) elastic recovery of ≥90%, (7) ambient photo- and thermal stability (resistance to ageing) and (8) tunable mechanical gradients with ≤500-µm resolution. This list is neither absolute nor exhaustive, but it is based on (commercial) precedent in both processing parameters and material properties observed for single-component vat-based 3D printing[6–8] and inspiration from natural multimaterial objects[1–5]. The predominant strategies for multimaterial 3D printing are topology optimization[9],

[1]Department of Chemistry, The University of Texas at Austin, Austin, TX, USA. [2]McKetta Department of Chemical Engineering, The University of Texas at Austin, Austin, TX, USA. [3]Walker Department of Mechanical Engineering, The University of Texas at Austin, Austin, TX, USA. [4]These authors contributed equally: Ji-Won Kim, Marshall J. Allen. e-mail: zpage@cm.utexas.edu

https://doi.org/10.1038/s41563-025-02249-z

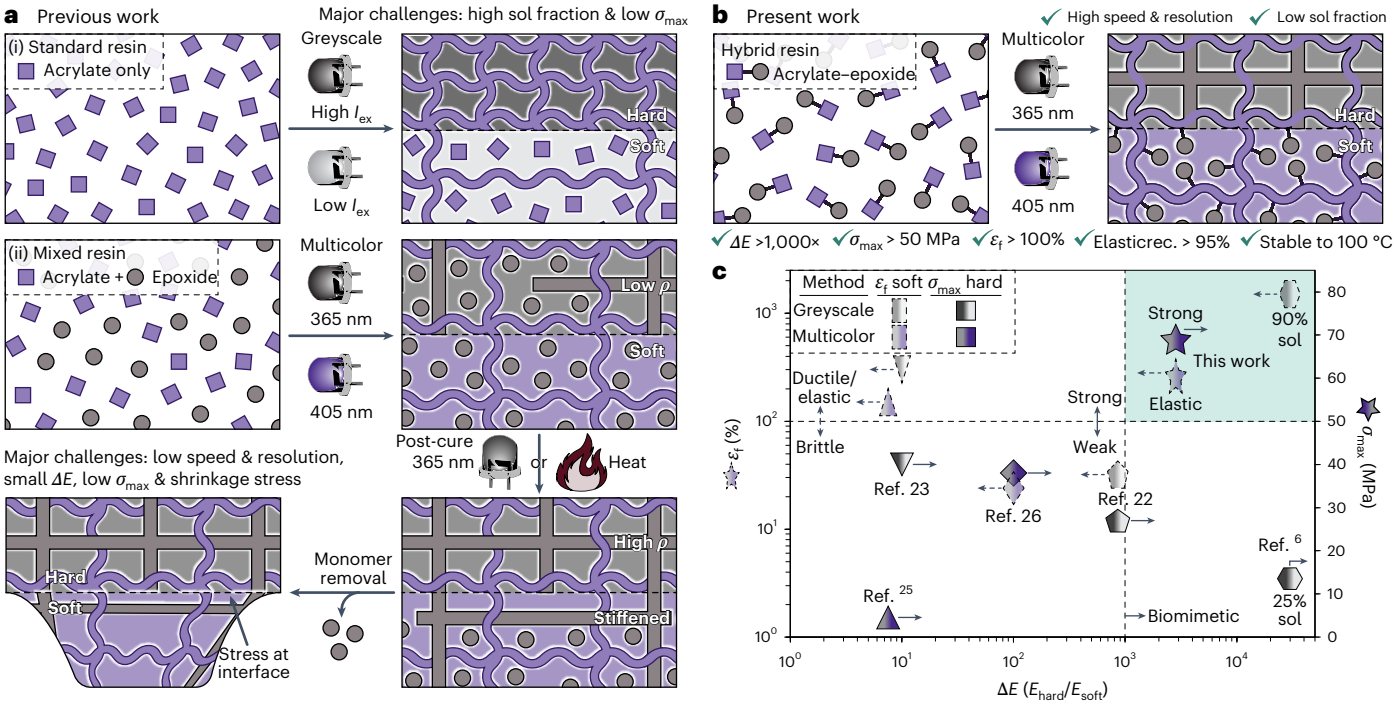

Fig. 1 | Comparison of past and present multimaterial 3D printing strategies. **a**, Previous approaches: (i) greyscale printing with acrylic resin, where unreacted monomer remains in low-light regions[21]; (ii) multicolour printing with mixed epoxy–acrylate resin, with post-curing for rigidity[25,26] and monomer removal leading to shrinkage. **b**, Present approach: multicolour printing with a hybrid epoxy–acrylate resin, achieving high print rates, covalent bonding between functionalities and large mechanical property variations with minimal sol fraction. **c**, Key examples of multimaterial 3D-printed structures and representative mechanical properties[22,23].

multinozzle extrusion[10,11], multimaterial jetting[12–14], multistep direct ink writing[15,16] and multivat[17–20], multidose[21–24] or multicolour[25–28] stereolithography. However, to date, no one strategy has addressed more than five of these eight criteria[29]. Of the various techniques, single-vat digital light processing (DLP)—a form of stereolithography—provides the best combination of speed (up to ~10 mm min^{-1} in z) and resolution (features of <10 µm) at a low cost[30,31].

The computer-aided design of lattices via topology optimization represents a clever strategy to mimic multimaterial structures with spatially defined mechanical properties using only one material in a DLP-compatible single-vat approach[32–36]. However, inherent design constraints, such as minimum strut thickness used to reduce bulk modulus (stiffness) has impeded implementation in applications with tight geometric tolerances and those requiring seamless hard/soft interfaces, such as biomedical devices or wearable electronics[37,38]. Multimaterial 3D printing via dosage-controlled (that is, greyscale) and spectrally controlled (that is, multicolour) photocuring offers an avenue to programme mechanical properties without altering geometry or introducing voids[21–28].

Greyscale 3D printing, in which light intensity is varied spatially within each slice to control local gel fraction and crosslink density, has also been leveraged as a versatile strategy to produce multimaterial objects (Fig. 1a(i))[21–24]. Qi and coworkers used greyscale DLP 3D printing with an acrylic-based resin to control local gel fraction, achieving an impressive ΔE of ~30,000-fold (0.016 to 480 MPa) with rapid build speeds (1 mm min^{-1}) and ~200-µm resolution[21]. However, the high sol fraction in soft domains (up to 90 wt%) raises stability and toxicity concerns due to leaching of unreacted monomers (Fig. 1a(i)). In parallel, Wallin and coworkers used greyscale patterning with a thiol-ene–epoxy resin to control thiol consumption and latent epoxy crosslinking, achieving stable objects with low sol fractions and ΔE > 4,000-fold (0.4 to 1,600 MPa) after post-baking[23]. However, poor structural integrity in undercured soft domains limited additive manufacturing, reducing the achievable ΔE in 3D-printed structures to ~10-fold (160 to 1,600 MPa).

Unlike greyscale photocuring, multicolour photocuring leverages differences in photon energy across wavelengths to drive distinct chemical reactions, enabling spatial control over chemical composition, gel fraction and crosslink density (Fig. 1a(ii))[39,40]. This approach creates spectrally responsive resins that are in essence pluripotent, as exposure to different colours of light results in the local formation of chemically diverse materials[41]. Spectrally responsive resins to prepare all-polymer multimaterial composites via lithography have been demonstrated via photocontrolled polymerizations[42–45], along with photocyclizations[46–48]. However, long development times (~minutes to hours) for a single layer often preclude implementation in 3D printing. Multicolour photoinitiation offers a faster alternative to photocontrolled polymerizations for curing acrylate–epoxy resin blends[25,26,49] (Fig. 1a(ii)). However, achieving wavelength-selective multimaterial 3D printing with the speed, resolution and mechanical tunability of greyscale methods remains challenging. Schwartz and Boydston used multicolour 3D printing to cure dual acrylate–epoxy resins, with visible light initiating radical acrylate curing and UV (365 nm, 0.75 mW cm^{-2}) triggering both cationic epoxy and radical acrylate curing[25]. However, ΔE was limited (~7.5-fold, from 10 to 75 MPa), and the printing speed was ≤0.10 mm min^{-1} (60–120 s per 100-µm layer). Later, Schlögl and coworkers achieved faster printing (1.5 mm min^{-1}) using a more reactive acrylate–epoxy resin and a higher-intensity DLP system (8 mW cm^{-2} at 405/365 nm)[26]. However, low epoxy conversion (<10%) required a 2-h post-bake at 120 °C, resulting in brittle parts (soft-material strain at break, ε_f < 50%), a ΔE of ~100-fold (20 to 2,000 MPa) and limited mechanical resolution. In all multicolour 3D printing cases, cationic epoxy curing is rate limiting, due in part to weak photoacid generator absorption at DLP wavelengths (365–405 nm). Additionally, green parts retain high sol fractions of unreacted epoxy, requiring solvent washing that causes shrinkage, embrittlement, stiffening and stress build-up,

especially at multimaterial interfaces—effects previously observed for dental resins[50,51] (Fig. 1a(ii)).

Here we overcome key challenges in multicolour DLP 3D printing with resins containing a hybrid acrylate–epoxy monomer and a UV-absorbing sensitizer. The hybrid monomer mitigates sol fractions while increasing ΔE, and the sensitizer enhances wavelength selectivity and epoxy polymerization rate, improving build speed and multimaterial resolution (Fig. 1b). As a result, build speeds up to 1.5 mm min^{-1}, sol fractions of <2.5 wt%, ΔE of ~3,000-fold (0.6 to 1,700 MPa), hard-material strength (σ_m) of ~69 MPa, ε_f > 250%, elastic recovery of ≥90%, hysteresis loss of <4% (100% strain), stability under UV (360 J cm^{-2}) and high temperatures (>100 °C), and mechanical gradients resolved to ~200 µm were demonstrated (Fig. 1c). The precision and potential utility were showcased by fabricating bioinspired structures with hard spring-like coils for damping (for example, vertebral spines) and smooth joints for seamless motion (for example, human knees)[52], as well as stretchable electronics leveraging large ΔE for targeted deformation.

Results and discussion

A hybrid acrylate–epoxy monomer, (3,4-epoxycyclohexyl)methyl acrylate (ECA), was chosen for wavelength-selective radical and cationic photocuring to access multimaterial thermosets (Fig. 2a). ECA was selected over other hybrid monomers, such as glycidyl methacrylate, to exploit cycloaliphatic epoxides' high reactivity towards cationic curing[53]. Type I photoacid generation was optimized for epoxy curing under UV radiation, while a type I radical photoinitiator enabled acrylate curing under violet or UV radiation (details below). This cross-reactivity was viewed as advantageous, as the persistent acrylate network could reinforce interfaces—common failure points in multimaterial structures[54]. Additionally, dual curing of hybrid acrylate–epoxy resins allowed for the incorporation of acrylate diluents to adjust resin viscosity, photocuring rate and material properties without excessive sol fractions; here 2-hydroxyethyl acrylate (HEA) and tetra(ethylene glycol) diacrylate (TEGDA) were employed (described below).

Photosystem optimization for spectral control using our initial 3D printing constraints (≤15 mW cm^{-2} at 365 nm, ≤80 mW cm^{-2} at 405 nm) was achieved via real-time Fourier transform infrared (RT-FTIR) spectroscopy to track monomer conversion (ρ). Seven industrial photoacid generators (aryl sulfonium and aryl iodonium salts) were screened with UV (365 nm) exposure (Supplementary Scheme 2, Supplementary Figs. 1–8 and Supplementary Table 4), while phenylbis(2,4,6-trimethylbenzoyl)phosphine oxide (BAPO) was selected as the violet (405-nm-)-light reactive radical photoinitiator (Fig. 2b). Photoacid generator testing used 3,4-epoxycyclohexylmethyl 3,4-epoxycyclohexanecarboxylate (ECC) as a proxy monomer due to overlapping epoxy and acrylate infrared absorption in ECA (Supplementary Fig. 1). Testing ECC alone confirmed that epoxide polymerization under ~10 mW cm^{-2} 365-nm light-emitting diode (LED) exposure was too slow for printing (>60 s to completion). Among candidates, bis[4-(diphenylsulfonio)phenyl]sulfide bis(hexafluoroantimonate) (THS) exhibited one of the fastest epoxide conversion rates and was selected for further experiments. Spectral overlap analysis (Fig. 2b, shaded regions) between each compound's absorbance and the 365/405-nm LED emissions informed wavelength-selective reactivity (Supplementary Figs. 9–13). Average molar absorptivity across full LED emission profiles was ~930 and 570 M^{-1} cm^{-1} for BAPO and ~150 and 12 M^{-1} cm^{-1} for THS at 365 and 405 nm, respectively (Supplementary Figs. 14–17 and Supplementary Table 5). Notably, the weak absorption of THS corresponded to slow epoxide polymerization (Supplementary Fig. 8).

To accelerate cationic polymerization, we examined photosensitizers with 365-nm absorption stronger than that of THS. Initially, 4-isopropylthioxanthone was tested due to its common use but it lacked selectivity, absorbing both 365- and 405-nm LEDs (Supplementary Fig. 16). We then used 3,6-dimethoxy-9*H*-thioxanthen-9-one (MeOTX), a blue-shifted photosensitizer with enhanced selectivity (molar absorptivities of ~1,920 M^{-1} cm^{-1} at 365 nm, ~13 times higher than that of THS, and 17 M^{-1} cm^{-1} at 405 nm; Fig. 2b and Supplementary Table 5), and developed a scalable two-step synthesis from commercial precursors (~80% yield; Supplementary Scheme 1 and Supplementary Figs. 18–21) to support systematic photocuring and 3D printing studies. Notably, MeOTX also improved UV versus violet absorption contrast (113-fold versus 12-fold for THS), which could promote selectivity.

Resin optimization was performed by tracking acrylate and epoxy conversion under UV and violet radiation using RT-FTIR spectroscopy (Fig. 2c, Supplementary Figs. 22–25 and Supplementary Tables 4 and 6). The optimized resin balanced polymerization speed, component solubility, viscosity and mechanical properties, and comprised ECA (67.9 mol%), BAPO (0.5 mol%), THS (1 mol%), MeOTX (0.5 mol%), HEA (30 mol%) and TEGDA (0.1 mol%). Samples were placed between 50-µm infrared-transparent plates to match printing conditions, and acrylate conversion was monitored via the disappearance of the sp^2 C–H stretch at 3,100 cm^{-1} (ref. 55). Upon 365- or 405-nm LED exposure (15 mW cm^{-2}), rapid polymerization occurred (rate = 1.5 ± 0.1 M s^{-1}), reaching 50% conversion in ~2 s (Fig. 2c and Supplementary Figs. 22–25), which also roughly corresponded to the gel point from photorheology (Supplementary Fig. 26), validating suitability for DLP 3D printing.

Epoxy polymerization was tracked using the C–O–C overtone stretch at 3,915 cm^{-1} and confirmed with the C–O–C stretch at 909 cm^{-1} (ref. 56) (Fig. 2d, Supplementary Figs. 1 and 26 and Supplementary Table 7). Due to signal convolution with acrylate functionality (Supplementary Fig. 1), a model acrylate-free resin comprising ECC (68 mol%), 3-ethyl-3-oxetanemethanol (OXA) (30 mol%), BAPO (0.5 mol%), THS (1 mol%) and MeOTX (0.5 mol%) was used to assess epoxy reactivity and photosystem selectivity. Like HEA in the hybrid resin, OXA improved photosystem solubility, reduced viscosity and accelerated epoxy polymerization by providing hydroxyl initiation sites. The photosystem selectively initiated epoxy polymerization under UV radiation but not violet light (15 mW cm^{-2}) over ~1 min (Fig. 2d and Supplementary Figs. 23–25). Limited epoxy conversion under UV exposure was attributed to early vitrification, which may differ in the hybrid resin due to acrylate diluents. Notably, OXA and MeOTX together increased the epoxy polymerization rate ~170-fold under UV radiation (Supplementary Table 4), achieving 0.17 ± 0.06 M s^{-1} and reaching 50% conversion in ~4 s, confirming suitability for DLP 3D printing.

Hybrid resins containing ECA (varied mol%), HEA (varied mol%), TEGDA (0.1 mol%), BAPO (0.5 mol%), THS (1 mol%) and MeOTX (0.5 mol%) were tested using a multicolour DLP 3D printer with 365- and 405-nm projectors (Fig. 3a). The projections were aligned through a dichroic filter, delivering ≥15 mW cm^{-2} at the build plane (~25-µm pixel resolution). Printing at 15 mW cm^{-2} for both wavelengths required 12 and 4 s per 50-µm layer of UV and violet radiation, respectively. Increasing intensities to 80 mW cm^{-2} (365 nm) and 40 mW cm^{-2} (405 nm) reduced exposure times to 2 and 1 s per 50-µm layer, respectively (Supplementary Fig. 39 and Supplementary Table 13), achieving *z*-build speeds of 0.25–1.5 mm min^{-1}. Resolution appeared insensitive to layering, as demonstrated with <50-µm features achieved across two to eight layers and 25–100-µm thicknesses (Supplementary Figs. 29 and 30 and Supplementary Tables 8 and 9). This result was supported by cure-depth working curves revealing ~300-µm thicknesses at 365 nm and ~800 µm at 405 nm under the applied dosages (Supplementary Figs. 31 and 32 and Supplementary Table 10).

To effectively remove residual monomers and photosystem components, we developed a washing procedure on the basis of swelling tests in isopropanol, ethyl acetate and acetone (Table 11). Isopropanol caused the largest swelling for 365-nm prints (~2%), while acetone led to the most swelling for 405-nm prints (~110%), with ethyl acetate intermediate for both. This was crucial for 405-nm prints to produce soft, plasticizer-free parts, precluding toxicity concerns and improving

https://doi.org/10.1038/s41563-025-02249-z

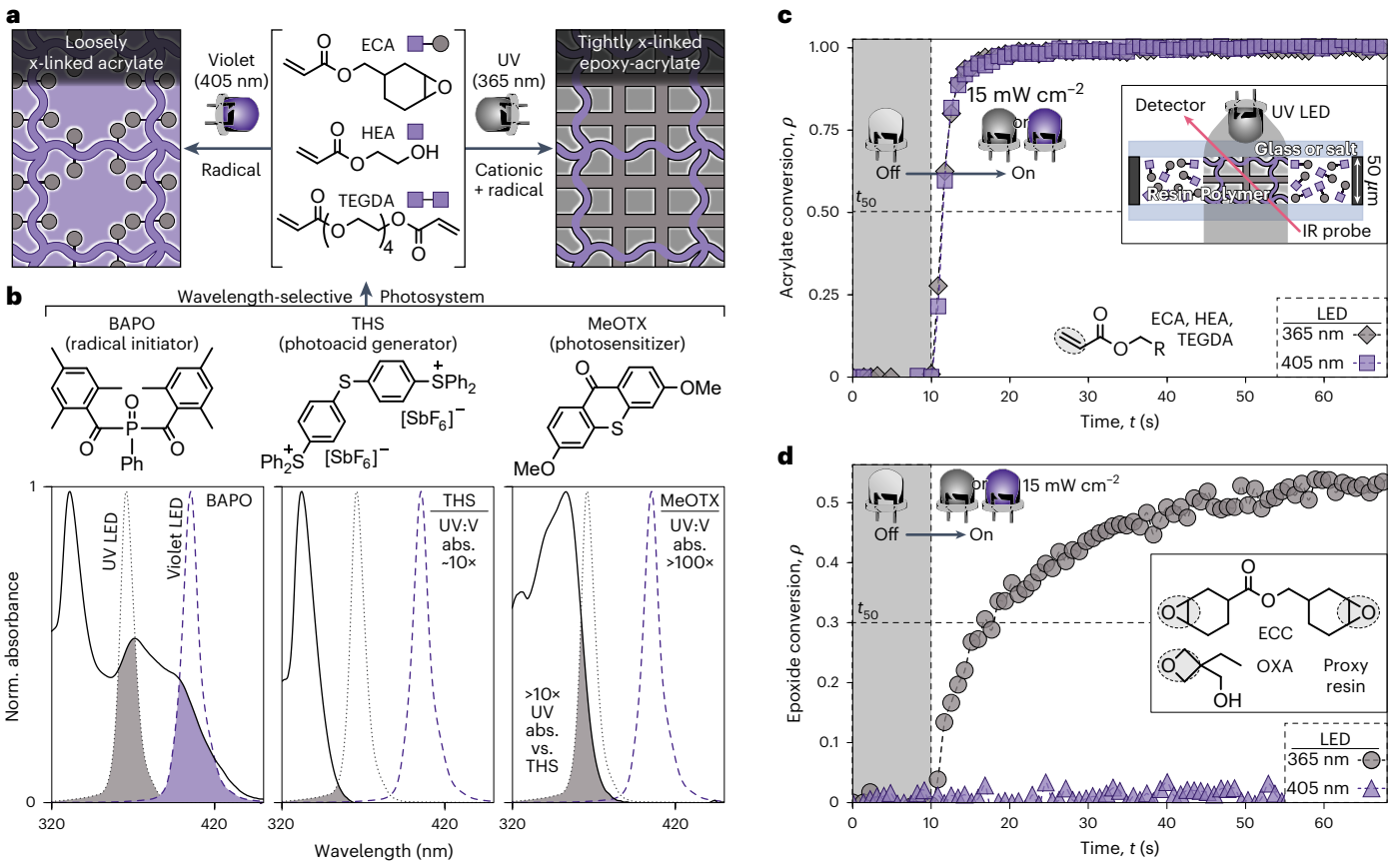

Fig. 2 | Resin components and wavelength-selective curing for multimaterial fabrication. a, Monomer structures and illustration of network formation under UV and violet LED exposure. **b**, Normalized absorbance profiles of photosystem components (solid black lines) and LED emission (dashed lines), with shaded regions indicating spectral overlap. **c**, RT-FTIR analysis of acrylate conversion (C=C–H, 3,100 cm^{-1}) in the hybrid resin: ECA (67.9 mol%), BAPO (0.5 mol%), THS (1 mol%), MeOTX (0.5 mol%), HEA (30 mol%) and TEGDA (0.1 mol%). **d**, RT-FTIR analysis of epoxy conversion (C–O–C, 3,915 cm^{-1}) in the acrylate-free proxy resin: ECC (68 mol%), BAPO (0.5 mol%), THS (1 mol%), MeOTX (0.5 mol%) and OXA (30 mol%). RT-FTIR was performed on 50-µm-thick resin samples, with LED irradiation (15 mW cm^{-2}) starting 10 s after measurement began.

ageing resistance. The optimized washing process revealed high gel fractions of ~99 ± 0.2 wt% (365 nm) and ~89 ± 1 wt% (405 nm) for 3D-printed green bodies (Supplementary Figs. 33 and 34 and Supplementary Table 12), while thermogravimetric analysis (TGA) confirmed effective solvent removal after vacuum drying.

3D-printed dogbone specimens for tensile testing exhibited distinct colours on the basis of curing light: yellow with UV and colourless with violet (Fig. 3b and Supplementary Figs. 35–38), aiding resolution characterization. In preparing these specimens resin optimization was performed by adjusting the HEA:ECA molar ratio and light exposure time while keeping light intensity (15 mW cm^{-2}) and layer thickness (50 µm) constant (Supplementary Figs. 39–45 and Supplementary Tables 13–17). A 3:7 HEA:ECA ratio with 12-s UV or 4-s violet exposure resulted in a ~3,000-fold difference in elastic modulus (ΔE). UV-cured samples formed stiff, strong plastics with an E of 1,700 ± 140 MPa, maximum strength (σ_m) of 69 ± 6 MPa and ε_f of 8 ± 2% after washing and drying (Fig. 3b, Supplementary Fig. 46 and Supplementary Table 18). In contrast, violet-light-printed samples were soft and extensible, with E = 0.60 ± 0.09 MPa, σ_m = 0.78 ± 0.05 MPa, ε_f = 260 ± 40% and Shore A hardness of 30.0 ± 0.8 (Table 19).

The photostability of printed samples was evaluated next due to the presence of labile epoxy groups that could compromise mechanical performance, especially in the soft materials. Accelerated ageing was accomplished via high-dosage UV exposure after printing (365 nm, 360 J cm^{-2}). Samples printed with UV radiation retained their mechanical properties (E = 1,700 ± 77 MPa, Supplementary Figs. 42 and 44 and Supplementary Table 15). However, violet-light-printed samples rinsed only with isopropyl alcohol stiffened ~600-fold after UV exposure (E = 940 ± 190 MPa, Supplementary Fig. 46 and Supplementary Table 18). In contrast, acetone-washed samples showed no substantial stiffness change (E = 0.57 ± 0.06 MPa, $n \geq 6$, coefficient of variation <16%, $P > 0.6$ for all pairwise comparisons) (Fig. 3b, dashed line, Supplementary Figs. 44 and 45 and Supplementary Table 15). These results suggest that acetone washing effectively removes the photoacid generator, providing a simple method to produce photostable elastomers.

The elasticity of the soft material was evaluated using cyclic tensile testing. Samples were stretched to 100% strain and unloaded to zero stress for 100 cycles at an initial strain rate of 3 × 10^{-3} s^{-1} (Fig. 3c), after preconditioning[57] with three loading–unloading cycles (Supplementary Fig. 47). Notably, violet-light-printed samples exhibited >99% elastic recovery with a low hysteresis loss of ~3–4%. For comparison, natural rubber, tested under identical conditions, also showed >99% recovery but had a hysteresis loss more than twice as high (~7–13%) due to strain-induced crystallization[58]. To further assess elastic recovery, compression testing following ASTM D395 conditions was performed. A cylindrical disc (13-mm diameter, 6-mm height) was compressed to 20% strain and held for 24 h (Supplementary Fig. 48). After unloading and re-equilibration, the sample recovered 90 ± 1% of its original shape, further demonstrating the elasticity and stability of the soft material.

The thermomechanical properties of 3D-printed parts were analysed using TGA, differential scanning calorimetry (DSC), dynamic

https://doi.org/10.1038/s41563-025-02249-z

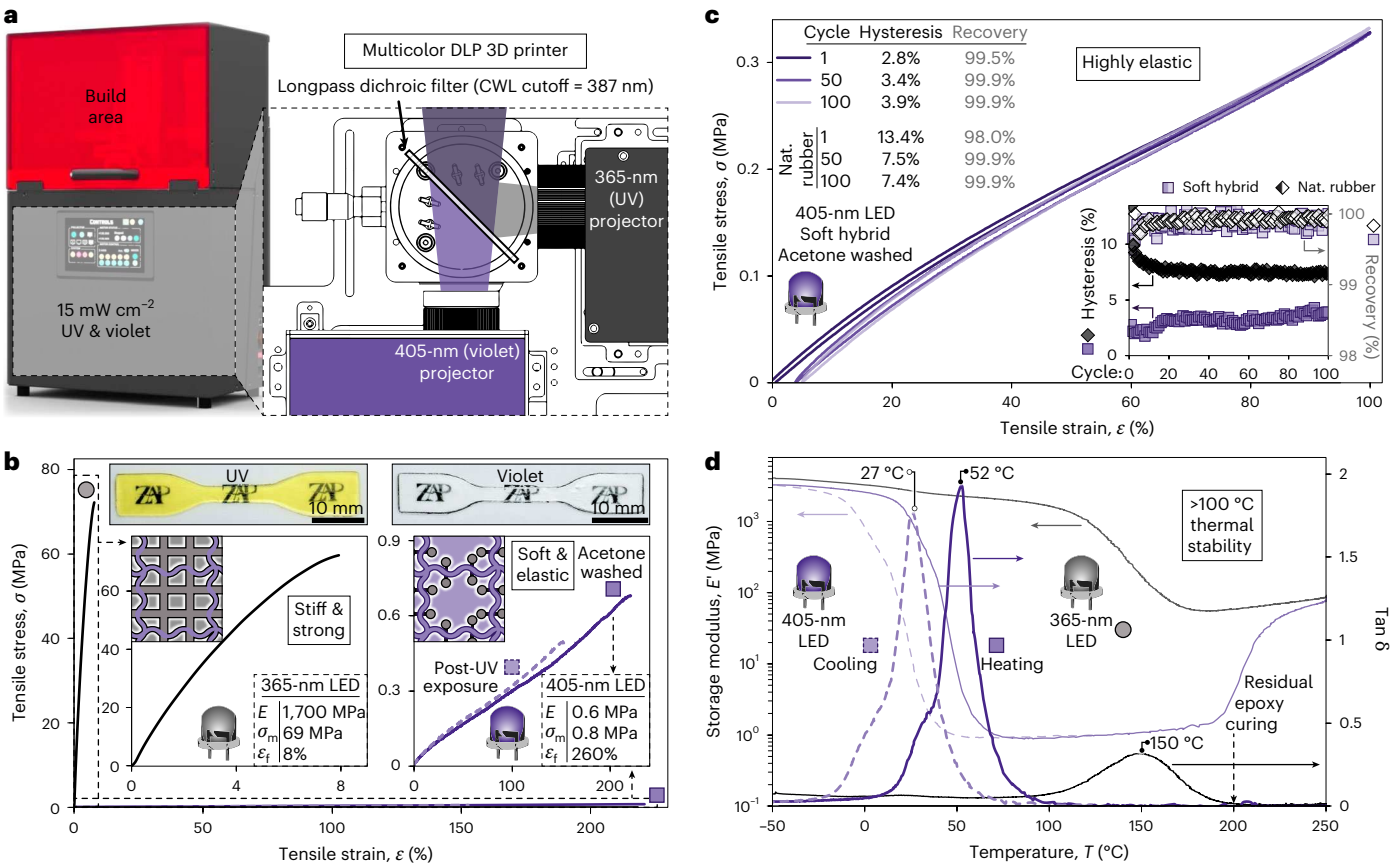

Fig. 3 | Colour-controlled DLP 3D printing and thermomechanical characterization of test bars. a, Schematic of a multicolour DLP 3D printer using UV (365-nm) and violet (405-nm) LEDs combined through a longpass dichroic filter. **b**, Stress–strain curves for hard (UV-printed) and soft (violet-printed) dogbones, with inset images (dimensions: 20 × 4 × 0.5 mm^3). Soft samples were acetone-washed (solid purple line) and post-irradiated with 360 J cm^{-2} UV radiation (dashed light-purple line) to assess photostability. Inset values are averages ($n \geq 7$). **c**, Representative stress–strain curves for soft dogbones under cyclic loading (initial strain rate: 3×10^{-3} s^{-1}). Inset: hysteresis and elastic recovery over 500 cycles, compared with natural rubber. **d**, Storage modulus and tan δ curves from DMA during heating and cooling (0.1% strain, 0.5 Hz).

mechanical analysis (DMA) and linear amplitude oscillatory shear rheology (Supplementary Figs. 49 and 56). TGA confirmed the removal of volatile components (for example, solvent, monomer) after washing and drying, with a 5-wt%-loss decomposition temperature ($T_{d5\%}$) above 330 °C for both hard and soft samples (Supplementary Fig. 49). DSC provided glass transition temperature (T_g) values of ~140 °C for UV-printed samples and ~18 °C for violet-light-printed samples (Supplementary Fig. 50). Notably, violet-light-printed samples displayed an exotherm around 200 °C, which was attributed to thermal epoxy curing (Supplementary Fig. 51).

DMA was used to examine the viscoelastic properties of the two materials (Fig. 3d and Supplementary Fig. 52). Similarly to DSC, heating and cooling cycles were applied under oscillatory tension (0.1% strain, 0.5 Hz) to erase thermal history and assess stability. Heating soft samples to 125 °C sharpened tan δ curves, which became highly dissipative upon cooling, peaking at ~2 near T_g (~27 °C). Given the viscoelastic nature of the soft material, time–temperature superposition was used to analyse its response across a wide frequency range (Supplementary Figs. 53 and 54). DMA and shear rheology confirmed viscoelastic behaviour at room temperature, transitioning to elastic-dominated behaviour at ≥35 °C or lower frequencies (≤0.1 Hz at 25 °C). Temperature step–sweep experiments in shear showed no hysteresis upon heating and cooling, with a plateau modulus (G') of 0.30 MPa at 25 °C, consistent with tensile testing (Supplementary Fig. 55). In contrast, UV-printed (hard) samples exhibited a peak tan δ of ~0.3 at 150 °C. Notably, above 200 °C, the soft material's E' matched the rubbery E' of the hard material, indicative of thermally activated epoxy crosslinking. However, shear rheology up to 80 °C and DMA step–sweep experiments (100–180 °C, 10-min holds) showed no substantial E' change below 120 °C and $E' < 1$ MPa up to ~180 °C (Supplementary Fig. 56), demonstrating thermal resistance. The resin's versatility was further shown by incorporating *n*-octyl acrylate as a reactive diluent, which lowered T_g from 18 to 4 °C (DSC) while maintaining $\Delta E \approx 1{,}500$-fold (Supplementary Figs. 57 and 58 and Supplementary Table 20). Overall, optimized soft (violet-light-printed) hybrid epoxy–acrylate objects exhibited high tan δ values, broad frequency-dependent behaviour, good thermal stability and compositional versatility, supporting their potential for energy absorption applications.

Resolution of multimaterial prints was evaluated optically and mechanically using colour contrast, tensile testing and nanoindentation. Samples with alternating UV- and violet-exposed lines (5-mm to 0.1-mm spacing) were 3D printed and imaged via light microscopy, which revealed sharp features down to 0.25 mm (Fig. 4a). To compare experimental moduli with an ideal composite spring model, uniaxial tension was applied to these samples with lines oriented parallel (∥) or perpendicular (⊥) to the deformation direction (Fig. 4b). At a 1:1 hard-to-soft ratio, theoretical tensile moduli were 850 ($E_\parallel$) and 1.2 MPa ($E_\perp$), independent of feature size. Experimentally, prints with ≥1-mm lines aligned well with predictions (Fig. 4a equation, Fig. 4b dashed lines and Supplementary Fig. 59). For instance, 1-mm lines yielded $E_\parallel = 956 \pm 2$ MPa and $E_\perp = 2.2 \pm 0.3$ MPa. However, as spacing decreased from 1 mm to 0.1 mm, series moduli increased, deviating

https://doi.org/10.1038/s41563-025-02249-z

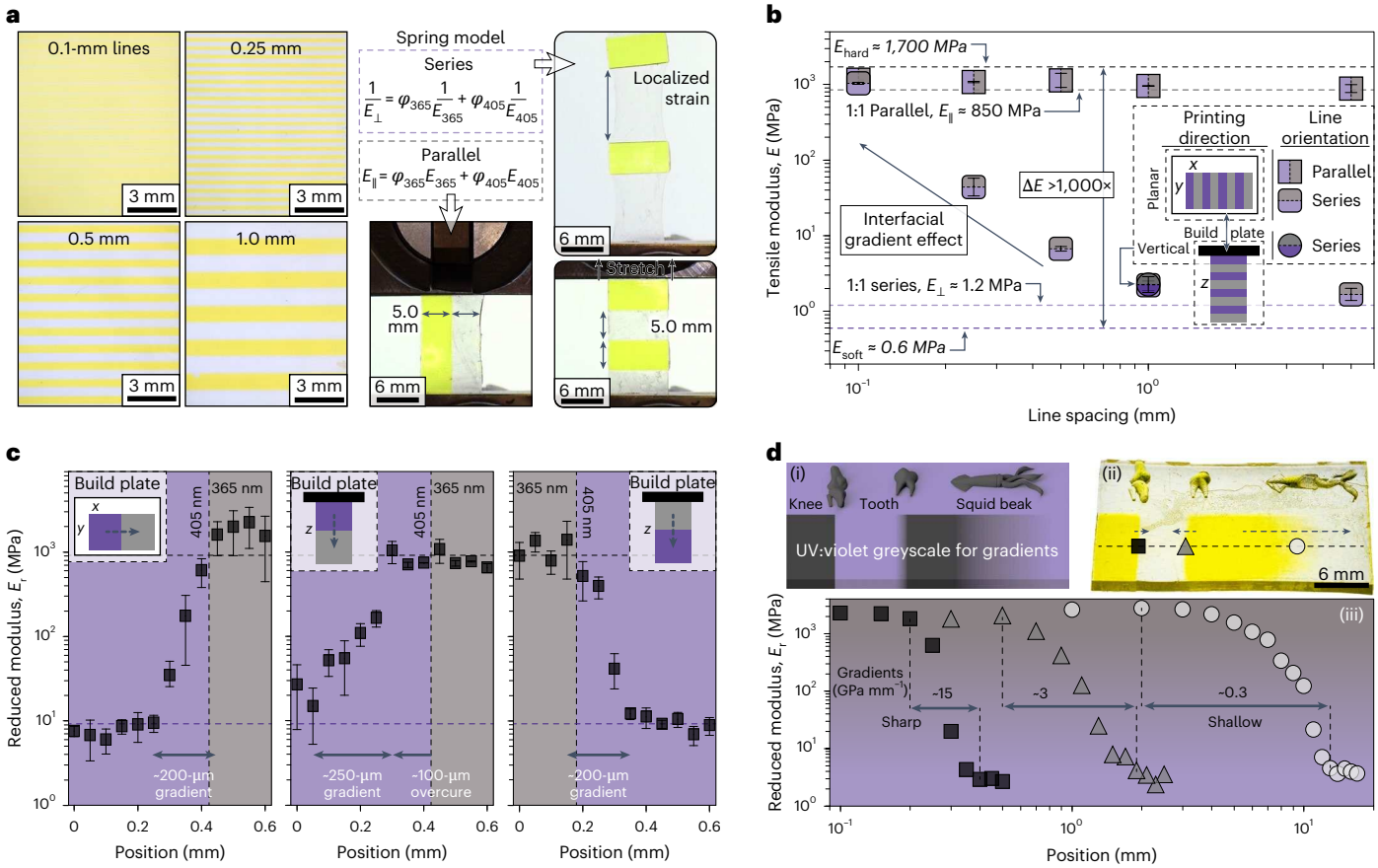

Fig. 4 | Resolution and mechanical characterization of 3D-printed multimaterial objects. a, Light-microscopy images of printed structures with soft–hard lines of varying widths, composite spring equations for series and parallel arrangements, and tensile testing of samples with 5-mm lines. $E_{\perp}$, series composite modulus; $E_{\parallel}$, parallel composite modulus; φ_{365}, hard volume fraction; φ_{405}, soft volume fraction; E_{365}, hard tensile modulus; E_{405}, soft tensile modulus. **b**, Measured tensile moduli for parallel and series orientations, with dashed lines indicating theoretical values. Data are presented as mean values ($n = 3$) ± s.d. **c**, Nanoindentation across soft–hard interfaces within a single layer (left) and between layers where soft layers were printed before (centre) or after (right) hard layers. Indentations were performed every 50 µm. Data are presented as mean values ($n \geq 10$) ± s.d. **d**, Programmable soft–hard interfaces mimicking natural stiffness gradients in knee entheses, tooth enamel and squid beaks using greyscale-controlled UV and violet-light exposure. (i) Digital model, (ii) printed sample and (iii) nanoindentation results.

from the model, converging with $E_{\parallel}$ at 0.1 mm probably due to UV overcure effects becoming more pronounced at higher soft–hard interfacial areas.

Nanoindentation was used to map stiffness across soft–hard interfaces in 3D-printed samples with lateral (x, y) and vertical (z) transitions (Fig. 4c). In all cases, contact modulus increased by around three orders of magnitude across the interface, consistent with tensile testing results. Laterally, the stiffness gradient spanned ~200 µm (slope ~8,500 MPa mm^{-1}, Fig. 4c left), comparable to recently reported 2D mechanical patterning[23,42,59,60]. This transition probably resulted from acid diffusion, light scattering and/or exothermic epoxy curing near illuminated regions. In contrast, printing hard layers onto soft ones created a broader ~250-µm gradient with ~100 µm of UV-induced overcure into soft layers (Fig. 4c centre), which was attributed to light transmission through active layers. However, when hard layers were printed first, followed by soft layers, the gradient remained ~200 µm (Fig. 4c right).

To emulate natural structures required programming interfacial gradients from sharp (~µm, as in knee entheses[61]) to shallow (~mm–cm, as in tooth enamel[62] or squid beaks[63]). We achieved this by overlaying greyscale UV and violet-light projections (Supplementary Fig. 60). Dogbones were 3D printed with simultaneous UV and violet exposure at varying intensity ratios (10:90 to 90:10, maximum 5 mW cm^{-2}; Supplementary Figs. 61 and 62), yielding mechanical properties intermediate between those for UV- and violet-only curing. Using this approach, we spatially programmed three distinct mechanical gradients into a 3D-printed bar (30 × 20 × 5 mm^3) by varying violet (5 to 0 mW cm^{-2}, 5 s per layer) and UV (0 to 5 mW cm^{-2}, 15 s per layer) intensities in the same direction (Fig. 4d). The resulting gradients matched those of a knee, tooth and squid beak, spanning around three orders of magnitude in reduced modulus ($E_r \approx 2$–2,000 MPa). From left to right, gradient slopes measured ~15, ~3 and ~0.3 GPa mm^{-1}, extending ~0.2, 1 and 10 mm, respectively. This multicolour greyscale DLP 3D printing method enables precise mechanical gradients within multimaterial objects.

To demonstrate the utility of multimaterial 3D printing for bioinspired mechanical metamaterials, we fabricated structures with unique bulk mechanical properties (Fig. 5 and Supplementary Figs. 63–70). Two key examples include (1) hard springs within soft cylinders to tune compressive damping (mimicking vertebrate spines) and (2) hard 'bones' connected by soft 'ligaments' for smooth joint articulation (as in human knees). For the first case, tunable compression was achieved without altering geometry or introducing voids by embedding a hard, twisted coil ('spring') of varying pitch (Fig. 5a and Supplementary Videos 1, 2, 3, 4 and 5) and diameter (Supplementary Figs. 63–65 and Supplementary Videos 6, 7 and 8) within a soft cylinder. Hard discs at the top and bottom displayed interfacial strength, with a lack of delamination under high stress and strain. Controls included a hard-only spring and a soft-only cylinder (with

https://doi.org/10.1038/s41563-025-02249-z

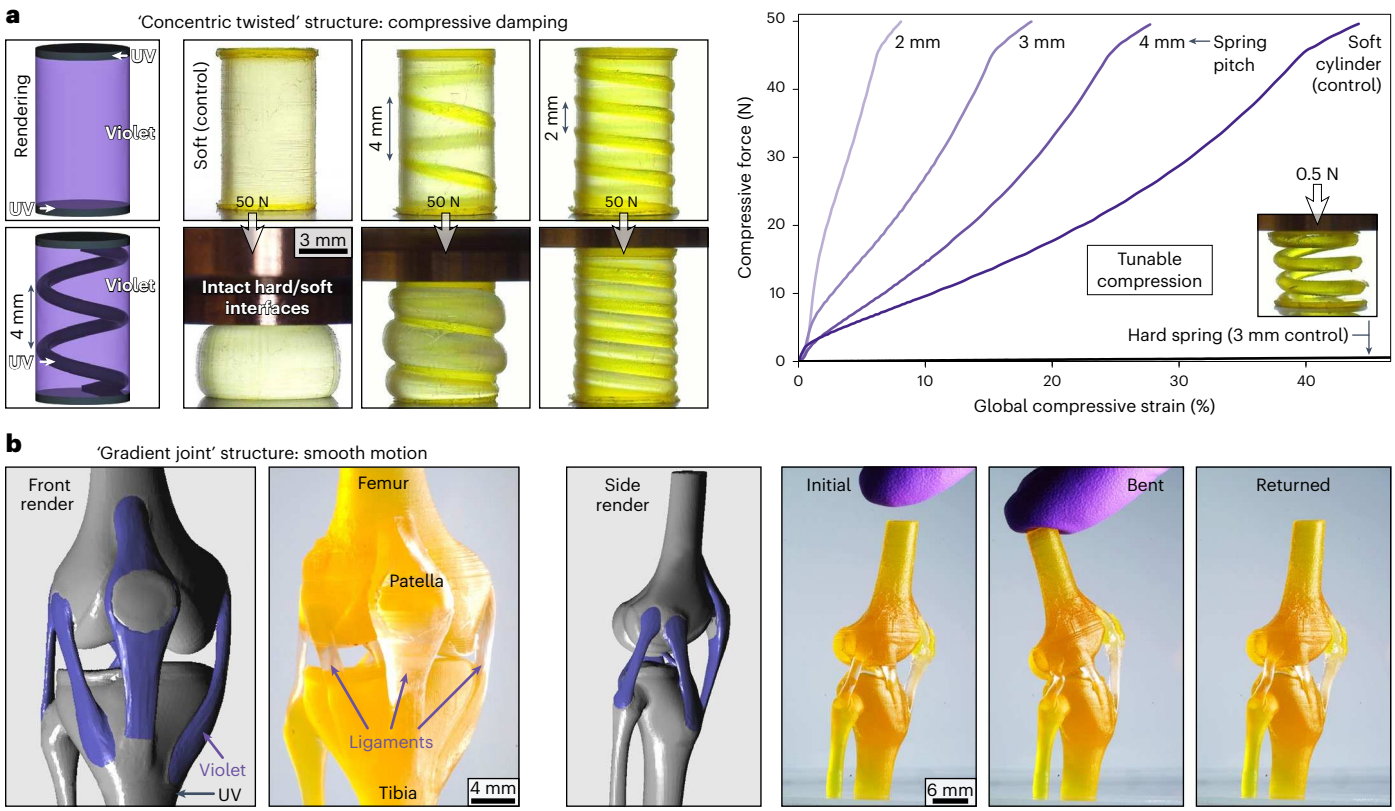

Fig. 5 | Multimaterial 3D printing of bioinspired mechanical metamaterials. **a**, Hard springs embedded in a soft cylinder, mimicking vertebrate spines to control compressive damping. Left: renderings and images of 3D-printed structures. Right: force–displacement curves compared with soft-cylinder and hard-spring controls. Inset: hard spring with a 3-mm pitch compressed to 45% strain. **b**, 3D-printed knee joint with rigid bones (femur, patella, tibia) and flexible ligaments. Renderings and images show smooth, reversible motion in one direction.

hard discs). Compression testing at 0.01 mm s^{-1} (0.1% s^{-1}) revealed pitch-dependent stiffness, increasing approximately fourfold as pitch decreased from 4 to 3 to 2 mm. At 50 N, compressive strains were 28%, 18% and 8%, respectively. In comparison, the soft-cylinder control reached 44% strain at 50 N, while a hard-only spring (3 mm pitch) compressed to 65% strain under just 1–2 N. These results highlight the nonlinear mechanical behaviour of multimaterial structures and the broad design possibilities enabled by this approach.

In a second example, a scaled-down human knee joint was 3D printed (Fig. 5b). The rigid femur, patella and tibia were fabricated using UV radiation, while soft, stretchable tendons and ligaments were simultaneously printed with violet light. The full structure measured ~46.5 mm high and ~17.5 mm wide at the knee, with the smallest features (ligaments/tendons) being ~0.6 mm in diameter. Despite their small size and proximity to larger rigid regions, the soft features remained intact and properly anchored. The high print fidelity allowed smooth, unidirectional bending with gentle hand pressure, followed by elastic retraction upon release (Fig. 5b, Supplementary Figs. 66 and 67 and Supplementary Video 9). This demonstrates the ability of multimaterial 3D printing to create lifelike joints with natural motion. Additional cylindrical structures demonstrated tunable mechanical properties through multimaterial design (Supplementary Figs. 68–70 and Supplementary Video 10). A layered soft–hard disk architecture, inspired by beetle forewings[52], enabled >10-fold stiffness variation by adjusting the width of soft rings without changing overall dimensions. A brick-and-mortar structure, mimicking nacre in shells[4], featured UV-printed hard 'bricks' embedded in a violet-light soft matrix, allowing strain energy density modulation by varying the number, placement and shape of hard inclusions. These examples showcase precise control over bulk mechanics without altering surface geometry.

To demonstrate the potential of this system for stretchable electronics, we designed multimaterial samples with controlled local deformation, leveraging a stiffness contrast (ΔE) > 1,000-fold with high elasticity (Fig. 6). Finite-element analysis (FEA) and digital image correlation (DIC) were used to evaluate strain distribution in ASTM II standardized dogbone samples with central inserts of varying stiffness (~1 MPa, '1×'; ~10 MPa, '10×'; ~100 MPa, '100×'; ~1,000 MPa, '1,000×') (Fig. 6a and Supplementary Figs. 74–78). FEA simulations showed that increasing insert stiffness reduced local strain under 30% global uniaxial strain to the following: ~4% for 10×, ~0.5% for 100× and ~0.05% for 1,000× (Fig. 6b and Supplementary Tables 3 and 21). DIC measurements confirmed these trends, with experimental strain values of 2.99%, 0.24% and 0.08% for 10×, 100× and 1,000× samples, respectively (Fig. 6c, Supplementary Figs. 79–82 and Supplementary Videos 11, 12 and 13). Notably, a ΔE of 1,000-fold reduced local strain below the fracture threshold of bulk silicon (<0.5%)[64], enabling designs that minimize deformation—a key feature for wearable electronics.

As a final proof of concept, stretchable electronic devices were created by depositing gold onto the central inserts of 1× and 1,000× samples and attaching a white LED (Fig. 6d). When stretched to 30% global strain, the 1× sample fractured, breaking the circuit and turning off the LED, while the 1,000× sample remained intact (Supplementary Videos 14 and 15). Gold-coated samples with intermediate stiffness (10× and 100×) were also tested without LEDs, measuring real-time resistance during stretching using a four-point probe. Resistance changes decreased as stiffness increased (Supplementary Fig. 83), highlighting improved electrical stability. These results demonstrate the potential of multimaterial 3D printing for advanced wearable electronics.

https://doi.org/10.1038/s41563-025-02249-z

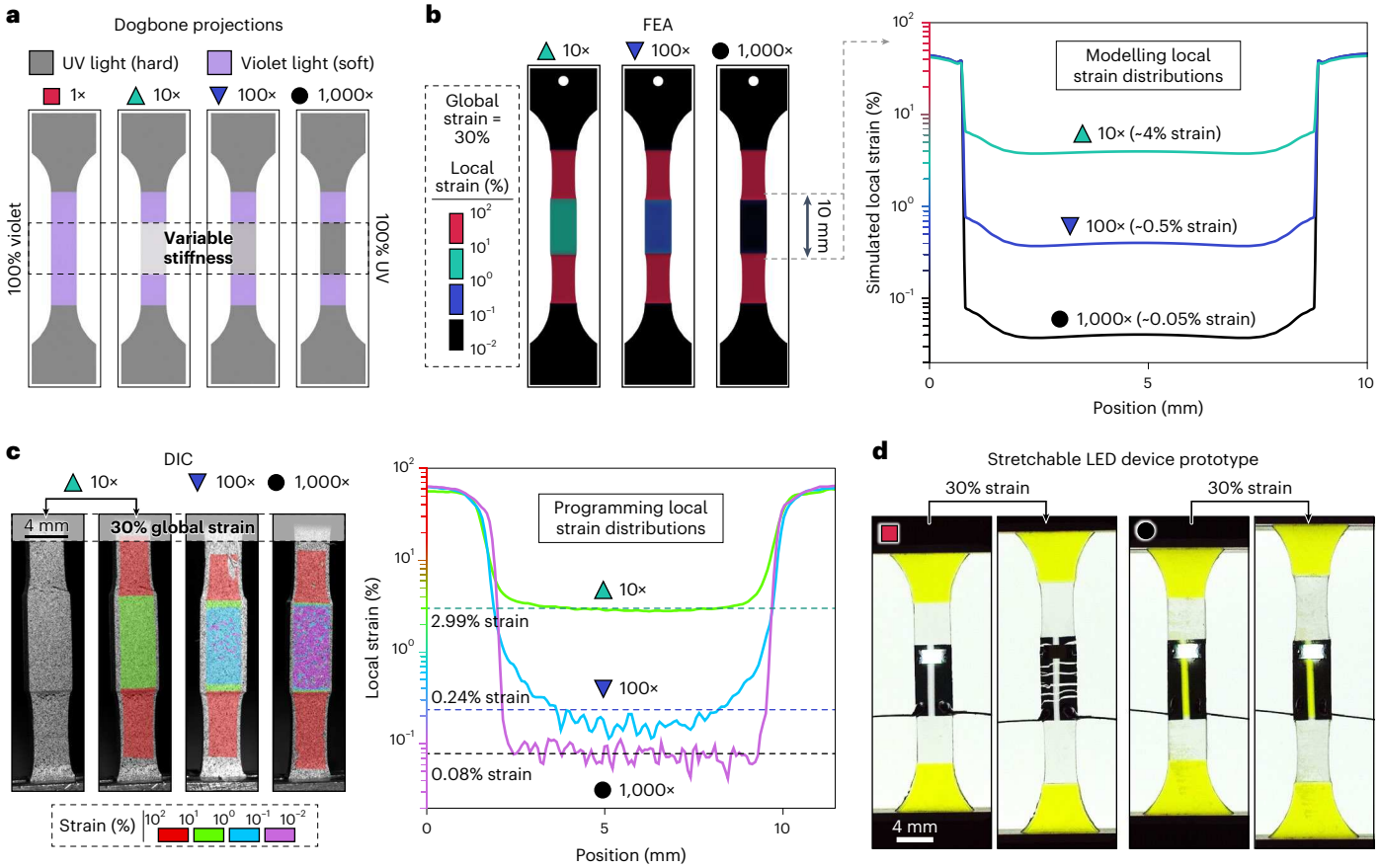

Fig. 6 | Local deformation in multimaterial tensile specimens and application in a stretchable electronic device. a, Schematic of UV and violet-light projections used to create dogbone samples with central inserts of varying tensile moduli (~1, ~10, ~100 and ~1,000 MPa), labelled as '1×', '10×', '100×' and '1,000×'. **b**, FEA simulations of 10×, 100× and 1,000× samples stretched to 30% global strain, showing colour-mapped strain distributions. **c**, Experimental strain mapping via DIC for samples at 30% global strain, with corresponding colour-mapped images and strain distributions. **d**, Images of 1× and 1,000× samples with mounted white LEDs before and after stretching, highlighting the need for a stiff insert to maintain functionality.

Concluding remarks

We have demonstrated a rapid, high-resolution, wavelength-selective 3D printing approach for fabricating multimaterial structures with extreme mechanical disparities, enabling bioinspired models and stretchable electronic devices. In creating hybrid epoxy–acrylate resins that contained an efficient photosystem to selectively trigger cationic and radical polymerizations, we achieved fast (up to 1.5 mm min^{-1}) printing of high-fidelity (~200-µm) multimaterial objects. These structures exhibited an unprecedented combination of $\Delta E \approx 3{,}000\times$, high strength ($\sigma_m \approx 69$ MPa), stretchability ($\varepsilon_f > 250\%$), elasticity (≥90% recovery with <4% hysteresis loss) and stability under high-intensity UV exposure and temperatures >100 °C. Greyscale multicolour projection enabled precise control over stiffness gradients at soft–hard interfaces, mimicking natural transitions from 0.2 to 10 mm. This level of precision is expected to advance applications in soft robotics, sealants, prosthetics and wearable health monitors, while also improving biological models for education and research. Despite these advantages, a key limitation of the current process is the need for extensive solvent washing to ensure long-term material stability. This challenge is particularly relevant for designs where soft materials are fully encapsulated within rigid structures, where new strategies to facilitate sol removal would be needed. Future work will explore alternative post-processing techniques, such as gas-phase amine ring-opening or hydrolysis, to overcome this limitation while enhancing material stability and expanding functional properties beyond mechanics, including thermal, electrical and optical tunability. Ultimately, this platform opens new frontiers in the fabrication of mechanical metamaterials, providing an experimental foundation to bridge gaps between theoretical predictions and real-world implementation.

Online content

Any methods, additional references, Nature Portfolio reporting summaries, source data, extended data, supplementary information, acknowledgements, peer review information; details of author contributions and competing interests; and statements of data and code availability are available at https://doi.org/10.1038/s41563-025-02249-z.

References

1. Ghazlan, A. et al. Inspiration from Nature's body armours—a review of biological and bioinspired composites. *Composites B* **205**, 108513 (2021).
2. Peisker, H., Michels, J. & Gorb, S. N. Evidence for a material gradient in the adhesive tarsal setae of the ladybird beetle *Coccinella septempunctata*. *Nat. Commun.* **4**, 1661 (2013).
3. Nazir, A. et al. Multi-material additive manufacturing: a systematic review of design, properties, applications, challenges, and 3D printing of materials and cellular metamaterials. *Mater. Des.* **226**, 111661 (2023).
4. Yang, Y. et al. Recent progress in biomimetic additive manufacturing technology: from materials to functional structures. *Adv. Mater.* **30**, 1706539 (2018).
5. Studart, A. R. Additive manufacturing of biologically-inspired materials. *Chem. Soc. Rev.* **45**, 359–376 (2016).

6. Montgomery, S. M., Demoly, F., Zhou, K. & Qi, H. J. Pixel-level grayscale manipulation to improve accuracy in digital light processing 3D printing. *Adv. Funct. Mater.* **33**, 2213252 (2023).
7. Bomar *3D Printing* https://bomar-chem.com/markets/3d-printing (2025).
8. Carbon *3D Printing Materials for Real-World Applications* https://www.carbon3d.com/materials (2025).
9. Mora, S., Pugno, N. M. & Misseroni, D. 3D printed architected lattice structures by material jetting. *Mater. Today* **59**, 107–132 (2022).
10. Skylar-Scott, M. A., Mueller, J., Visser, C. W. & Lewis, J. A. Voxelated soft matter via multimaterial multinozzle 3D printing. *Nature* **575**, 330–335 (2019).
11. Kokkinis, D., Bouville, F. & Studart, A. R. 3D printing of materials with tunable failure via bioinspired mechanical gradients. *Adv. Mater.* **30**, 1705808 (2018).
12. Zhou, L. et al. Multimaterial 3D printing of highly stretchable silicone elastomers. *ACS Appl. Mater. Interfaces* **11**, 23573–23583 (2019).
13. Mirzaali, M. J. et al. Mechanics of bioinspired functionally graded soft–hard composites made by multi-material 3D printing. *Compos. Struct.* **237**, 111867 (2020).
14. Buchner, T. J. K. et al. Vision-controlled jetting for composite systems and robots. *Nature* **623**, 522–530 (2023).
15. Peng, X. et al. Integrating digital light processing with direct ink writing for hybrid 3D printing of functional structures and devices. *Addit. Manuf.* **40**, 101911 (2021).
16. Armstrong, C. D. et al. A hybrid additive manufacturing process for production of functional fiber-reinforced polymer composite structures. *J. Compos. Mater.* **57**, 841–850 (2023).
17. Ge, Q. et al. 3D printing of highly stretchable hydrogel with diverse UV curable polymers. *Sci. Adv.* **7**, eaba4261 (2021).
18. Xu, Z. et al. Additive manufacturing of two-phase lightweight, stiff and high damping carbon fiber reinforced polymer microlattices. *Addit. Manuf.* **32**, 101106 (2020).
19. Cheng, J. et al. Centrifugal multimaterial 3D printing of multifunctional heterogeneous objects. *Nat. Commun.* **13**, 7931 (2022).
20. Han, D., Yang, C., Fang, N. X. & Lee, H. Rapid multi-material 3D printing with projection micro-stereolithography using dynamic fluidic control. *Addit. Manuf.* **27**, 606–615 (2019).
21. Yue, L. et al. Single-vat single-cure grayscale digital light processing 3D printing of materials with large property difference and high stretchability. *Nat. Commun.* **14**, 1251 (2023).
22. Kuang, X. et al. Grayscale digital light processing 3D printing for highly functionally graded materials. *Sci. Adv.* **5**, eaav5790 (2019).
23. Huang, S. et al. One-pot ternary sequential reactions for photopatterned gradient multimaterials. *Matter* **6**, 2419–2438 (2023).
24. Ma, Y. et al. Multimaterial thermoset synthesis: switching polymerization mechanism with light dosage. *ACS Cent. Sci.* **10**, 2125–2131 (2024).
25. Schwartz, J. J. & Boydston, A. J. Multimaterial actinic spatial control 3D and 4D printing. *Nat. Commun.* **10**, 791 (2019).
26. Cazin, I. et al. Spatially controlling the mechanical properties of 3D printed objects by dual-wavelength vat photopolymerization. *Addit. Manuf.* **57**, 102977 (2022).
27. Rossegger, E. et al. Wavelength selective multi-material 3D printing of soft active devices using orthogonal photoreactions. *Macromol. Rapid Commun.* **44**, 2200586 (2023).
28. Gaca, S., Dietliker, K., Rossegger, E. & Schlögl, S. Design of photocurable thiol–epoxy resins for the processing of vitrimers with vat photopolymerisation 3D printing. *React. Funct. Polym.* **205**, 106085 (2024).
29. Zhu, C., Gemeda, H. B., Duoss, E. B. & Spadaccini, C. M. Toward multiscale, multimaterial 3D printing. *Adv. Mater.* **36**, 2314204 (2024).
30. Chen, J. et al. 3D-printed anisotropic polymer materials for functional applications. *Adv. Mater.* **34**, 2102877 (2022).
31. Wallin, T. J., Pikul, J. & Shepherd, R. F. 3D printing of soft robotic systems. *Nat. Rev. Mater.* **3**, 84–100 (2018).
32. Abueidda, D. W. et al. Mechanical properties of 3D printed polymeric gyroid cellular structures: experimental and finite element study. *Mater. Des.* **165**, 107597 (2019).
33. Farzaneh, A., Pawar, N., Portela, C. M. & Hopkins, J. B. Sequential metamaterials with alternating Poisson's ratios. *Nat. Commun.* **13**, 1041 (2022).
34. Ubaid, J., Schneider, J., Deshpande, V. S., Wardle, B. L. & Kumar, S. Multifunctionality of nanoengineered self-sensing lattices enabled by additive manufacturing. *Adv. Eng. Mater.* **24**, 2200194 (2022).
35. Geiger, F., Kebbach, M., Vogel, D., Weissmann, V. & Bader, R. Efficient computer-based method for adjusting the stiffness of subject-specific 3D-printed insoles during walking. *Appl. Sci.* **13**, 3854 (2023).
36. Dwyer, C. M. et al. Impact performance of 3D printed spatially varying elastomeric lattices. *Polymers* **15**, 1178 (2023).
37. Libanori, R. et al. Stretchable heterogeneous composites with extreme mechanical gradients. *Nat. Commun.* **3**, 1265 (2012).
38. Wei, R. et al. Revolutionizing wearable technology: advanced fabrication techniques for body-conformable electronics. *npj Flex. Electron.* **8**, 83 (2024).
39. Ehrmann, K. & Barner-Kowollik, C. Colorful 3D printing: a critical feasibility analysis of multi-wavelength additive manufacturing. *J. Am. Chem. Soc.* **145**, 24438–24446 (2023).
40. Lu, P. et al. Wavelength-selective light–matter interactions in polymer science. *Matter* **4**, 2172–2229 (2021).
41. Boynton, N. R. et al. Accessing pluripotent materials through tempering of dynamic covalent polymer networks. *Science* **383**, 545–551 (2024).
42. Ma, Y. et al. Photoswitching cationic and radical polymerizations: spatiotemporal control of thermoset properties. *J. Am. Chem. Soc.* **143**, 21200–21205 (2021).
43. Shanmugam, S., Cuthbert, J., Kowalewski, T., Boyer, C. & Matyjaszewski, K. Catalyst-free selective photoactivation of RAFT polymerization: a facile route for preparation of comblike and bottlebrush polymers. *Macromolecules* **51**, 7776–7784 (2018).
44. Xu, J., Shanmugam, S., Fu, C., Aguey-Zinsou, K. F. & Boyer, C. Selective photoactivation: from a single unit monomer insertion reaction to controlled polymer architectures. *J. Am. Chem. Soc.* **138**, 3094–3106 (2016).
45. Zhao, Y., Ma, M., Lin, X. & Chen, M. Photoorganocatalyzed divergent reversible-deactivation radical polymerization towards linear and branched fluoropolymers. *Angew. Chem. Int. Ed.* **59**, 21470–21474 (2020).
46. Frisch, H., Marschner, D. E., Goldmann, A. S. & Barner-Kowollik, C. Wavelength-gated dynamic covalent chemistry. *Angew. Chem. Int. Ed.* **57**, 2036–2045 (2018).
47. Van De Walle, M., De Bruycker, K., Blinco, J. P. & Barner-Kowollik, C. Two colour photoflow chemistry for macromolecular design. *Angew. Chem. Int. Ed.* **59**, 14143–14147 (2020).
48. Bialas, S. et al. Access to disparate soft matter materials by curing with two colors of light. *Adv. Mater.* **31**, 1807288 (2019).
49. Dolinski, N. D. et al. Solution Mask Liquid Lithography (SMaLL) for one-step, multimaterial 3D printing. *Adv. Mater.* **30**, 1800364 (2018).
50. Mantri, S. P. & Mantri, S. S. Management of shrinkage stresses in direct restorative light-cured composites: a review. *J. Esthet. Restor. Dent.* **25**, 305–313 (2013).

51. Soares, C. J. et al. Polymerization shrinkage stress of composite resins and resin cements—what do we need to know? *Braz. Oral Res.* **31**, e62 (2017).
52. Ha, N. S. & Lu, G. A review of recent research on bio-inspired structures and materials for energy absorption applications. *Composites B* **181**, 107496 (2020).
53. Guy, N., Giani, O., Blanquer, S., Pinaud, J. & Robin, J.-J. Photoinduced ring-opening polymerizations. *Prog. Org. Coat.* **153**, 106159 (2021).
54. Dolinski, N. D. et al. Tough multimaterial interfaces through wavelength-selective 3D printing. *ACS Appl. Mater. Interfaces* **13**, 22065–22072 (2021).
55. Arivazhagan, G., Elangovan, A., Shanmugam, R., Vijayalakshmi, R. & Karthick, N. K. Study of molecular interaction in the mixtures of benzene+methyl acrylate/butyl acrylate through dielectric and spectroscopic studies. *J. Mol. Liq.* **214**, 357–363 (2016).
56. González, M. G., Cabanelas, J. C. & Baselga, J. in *Infrared Spectroscopy—Materials Science, Engineering and Technology* (ed. Theophile, T.) 261–284 (IntechOpen, 2012).
57. Creton, C., Hu, G., Deplace, F., Morgret, L. & Shull, K. R. Large-strain mechanical behavior of model block copolymer adhesives. *Macromolecules* **42**, 7605–7615 (2009).
58. Zhang, H. et al. Strain induced nanocavitation and crystallization in natural rubber probed by real time small and wide angle X-ray scattering. *J. Polym. Sci. B* **51**, 1125–1138 (2013).
59. Allen, M. J. et al. Multimorphic materials: spatially tailoring mechanical properties via selective initiation of interpenetrating polymer networks. *Adv. Mater.* **35**, 2210208 (2023).
60. Rylski, A. K. et al. Polymeric multimaterials by photochemical patterning of crystallinity. *Science* **378**, 211–215 (2022).
61. Abraham, A. C., Pauly, H. M. & Haut Donahue, T. L. Deleterious effects of osteoarthritis on the structure and function of the meniscal enthesis. *Osteoarthr. Cartil.* **22**, 275–283 (2014).
62. Lu, J. et al. Hierarchically mimicking outer tooth enamel for restorative mechanical compatibility. *Nat. Commun.* **15**, 10182 (2024).
63. Miserez, A., Schneberk, T., Sun, C., Zok, F. W. & Waite, J. H. The transition from stiff to compliant materials in squid beaks. *Science* **319**, 1816–1819 (2008).
64. Passi, V. et al. Note: Fast and reliable fracture strain extraction technique applied to silicon at nanometer scale. *Rev. Sci. Instrum.* **82**, 116106 (2011).

Methods

Additional experimental method details—materials, synthesis and instrumentation—are provided in Supplementary Information.

Materials

Chemicals. Photosensitizer synthesis: 2-bromo-4-methoxybenzoic acid (98%, Ambeed), 3-methoxybenzene thiol (>98.0%, TCI Chemicals), potassium carbonate anhydrous (lab grade, Fisher Scientific), copper powder (98%, Sigma-Aldrich), copper(I) oxide (97%, Sigma-Aldrich), 2-ethoxyethanol (99%, Sigma-Aldrich), sodium carbonate (98%, Thermo Scientific), celite filter aid (certified ACS, Fisher Scientific), oxalyl chloride (98%, Sigma-Aldrich), aluminium chloride (>98.0%, TCI Chemicals), dichloromethane (certified ACS, Fisher Scientific), dimethylformamide (≥99.9%, Sigma-Aldrich), hydrochloric acid (certified ACS plus, Fisher Scientific), sodium bicarbonate (certified ACS, Fisher Scientific), magnesium sulfate anhydrous (certified ACS, Fisher Scientific) and hexanes (certified ACS, Fisher Scientific) were used as received. Photoacid generators: HNu254 onium salt (Spectra), 4-octyloxydiphenyliodonium hexafluoroantimonate (pure HNu254, 98%, AA Blocks), 4-isobutylphenyl-4′-methylphenyliodonium hexafluorophosphate (Irgacure 250, 70%, AA Blocks), bis(4-tert-butylphenyl) iodonium hexafluorophosphate (98%, Sigma-Aldrich), triarylsulfonium hexafluoroantimonate salts (mixture, 50 wt% in propylene carbonate, Sigma-Aldrich), diphenyl[4-(phenylthio)phenyl]sulfonium hexafluoroantimonate (>98%, TCI Chemicals) and THS (95%, Combi-Blocks) were used as received. Other resin components: BAPO (97%, Sigma-Aldrich), 2-isopropylthioxanthone (97%, Sigma-Aldrich), ECC (97%, Ambeed), OXA (98%, SynQuest Laboratories), ECA (96%, Combi-Blocks), HEA (95%, Fisher Scientific) and TEGDA (>90%, TCI Chemicals) were used as received.

Resin formulation. The optimized 3D printing resin was prepared by mixing BAPO, THS, MeOTX (Supplementary Section 1.2), TEGDA, HEA and ECA (see Supplementary Table 1 for representative mixture). The mixture was sonicated for 30 min to ensure thorough mixing. The resin was either used immediately or else stored at −10 °C and then warmed to room temperature before future use. In experiments with variable HEA content, the mole fraction of ECA was altered to make up for the gain or loss of HEA from 30 mol%, while all other components remained as the stated mole percentages.

Post-print processing. All 3D-printed structures were rinsed with isopropanol immediately after printing, then soaked in a 500-ml beaker filled with solvent: isopropanol for hard materials (printed with 365-nm light), acetone for soft materials (printed with 405-nm light) and either isopropanol or ethyl acetate for multimaterial structures (as noted). For thorough washing of soft materials, each specimen was placed in a 20-ml amber vial filled with acetone and vortexed on a heated shaker at 650 r.p.m. at room temperature for ~24 h, then transferred to a Teflon plate and vacuum-dried (<0.15 mmHg) for two days before testing.

Instrumentation

Real-time Fourier transform infrared spectroscopy (RT-FTIR). Light-induced polymerizations were monitored in real time using FTIR spectroscopy (INVENIO-R, Bruker), controlled via OPUS spectroscopy software.

UV–visible spectroscopy. Absorptivity in the ultraviolet and visible (UV–vis) spectral regions for each of the photosystem components were characterized using UV–vis absorption spectroscopy (QE PRO-ABS, Ocean Insight) with a deuterium–tungsten halogen light source (DH-2000-BAL, Ocean Insight). LED emission profiles and the dichroic mirror profile were collected using the same UV–vis spectrophotometer.

Nuclear magnetic resonance (NMR) spectroscopy. NMR spectra were recorded at room temperature on an Agilent MR spectrometer (400 MHz for ^{1}H NMR and 100 MHz for ^{13}C NMR) utilizing $CDCl_3$ as the solvent. ^{1}H NMR was carried out coupled and referenced to the $CDCl_3$ chemical shift at 7.26 ppm. ^{13}C NMR was carried out decoupled and referenced to the $CDCl_3$ chemical shift at 77.16 ppm. Data are reported as multiplicity (s, singlet; d, doublet; t, triplet; q, quartet; pent, pentet; m, multiplet).

High-resolution mass spectrometry. High-resolution mass spectrometry was performed on an Agilent Technologies 6530 Accurate-Mass Q-TOF LC/MS using electrospray ionization and the data were subsequently analysed using Agilent MassHunter Qualitative Analysis software.

Rheology. Rheology (Discovery HR2, TA Instruments) was used to determine viscosity and estimate the gel point for the 3D printing resins, and to conduct compression testing of 3D-printed multimaterial structures using a 20-mm upper parallel steel plate (TA Instruments). For linear amplitude oscillatory rheology, an Anton-Parr MCR302e rheometer was used with an 8-mm-diameter probe.

Two-channel 3D printing. 3D printing was performed using a custom-made, DLP-based 3D printer (MONO3MZ2, Monoprinter). The printer contained two LED projectors with wavelengths centred at 365 and 405 nm (PDC04-365 nm and PDC04-405 nm), combined through a dichroic mirror (T387lp, 35 mm × 50 mm × 1 mm, Chroma).

Universal tensile testing. A tensile tester (Autograph AGS-X, Shimadzu) equipped with TRAPEZIUM X software was used to measure Young's modulus, maximum stress, maximum strain, hysteresis and elastic recovery values of 3D-printed films under unidirectional stretching. The uniaxial testing of bulk films was performed on ASTM D638 type IV dogbones that were produced using a projection scaled to 30% of the original size: sample gauge length = 8.26 mm, width = 1.8 mm, thickness = 0.96 mm, total length = 34.5 mm.

Digital image correlation (DIC). Specimens were spray painted on one side with a layer of white airbrush paint and then a speckled layer of black paint (Timbertech Airbrush Kit with compressor AS18-2K ASIN B08FR765S4). Specimens were imaged using VIC-snap software (Correlation Solutions) with two Basler Ace cameras (acA4112-30um) simultaneously at 1 s^{-1} with a lens (LM35HC from KOWA) and two 5-mm lens extenders attached (CAMINSTARRY ASIN B09B6Y29QC).

Differential scanning calorimetry (DSC). DSC (DSC 2500, TA Instruments) was performed on samples (~20 mg) placed in a hermetic aluminium pan and sealed with a hermetic aluminium lid. Temperature ramping methods are detailed in the supporting information.

Thermogravimetric analysis (TGA). TGA (Q500, TA Instruments) was performed with samples (~10 mg) placed in a platinum pan and subjected to heating at a rate of 10 °C min^{-1} from room temperature to 820 °C under a nitrogen atmosphere.

Dynamic mechanical analysis (DMA). DMA (Q800, TA Instruments) was used to characterize T_g, viscoelastic properties and thermal stability in a tensile geometry along with elasticity in a compression geometry.

Nanoindentation. Nanoindentation of 3D-printed samples was carried out using a nanomechanical indent system (Hysitron TI 950 TriboIndenter, Bruker). Samples were loaded to a maximum force of 1,000 μN over a period of 10 s and unloaded over a 10-s period. The modulus was calculated using Hysitron software by fitting a slope to the unloading force–displacement curve.

Shore A hardness measurement. Shore A hardness measurements were performed with a handheld durometer (Gain Express Shore A durometer). Three cylinders 13 mm in diameter and 6 mm tall were pressed three times with the tip of the durometer to obtain the average hardness of the specimen.

Optical/digital microscopy. An optical microscope (Eclipse LV100ND, Nikon) was utilized to image photopolymerization reactions during LED irradiation. Additionally, a digital microscope (VHX-7000, Keyence and Edge WF4915ZT, Dino-Lite) was used to take optical images of 3D-printed structures.

Physical vapour deposition. ASTM dogbone samples were patterned via physical vapour deposition using a custom-built Kurt J. Lesker PRO Line PVD 75. Chromium and gold were the chosen evaporation materials, deposited through a shadow mask. The chromium layer accumulated to 5 nm, followed by 95 nm of gold.

Ansys FEA mechanical simulations. Mechanical finite-element methods were performed with Ansys Multiphysics 2023 R1 to correlate experimentally imposed mechanical strains with theoretical predictions. The devised finite-element method model followed Structural Physics, Static Structural Analysis and a Mechanical APDL solver under Ansys Mechanical. See Supplementary Information for the engineering data, material assignment details, simulation parameters, meshing, boundary conditions and analysis settings.

Resistance measurements. Resistance data were obtained using the Van der Pauw method with a Keithley 6220 Precision DC Source and a Keithley nanovoltmeter, with KI6220 software. A typical current of 20–200 μA was applied to account for variations in contact resistance. This set-up allowed for precise tracking of resistance changes in response to applied strain, ensuring high-quality data collection.

Electronic devices. To establish electrical connections between instruments and samples, ARCOR bare copper wire at 32 AWG (American wire gauge) was employed to connect the deposited gold to both the resistance measurement instruments and the direct current supply for the LED. The connections were made using MG Chemicals 8331D silver conductive epoxy adhesive, which is a two-part epoxy that was mixed freshly for each application. A Chanzon SMD LED was affixed near one end of the gold deposition. Its positive and negative leads were carefully bonded to the divided gold foil using the same silver epoxy, while the 32 AWG copper wire was adhered to the opposite end to facilitate the circuit connection to the power supply.

Data availability

The data supporting the findings of this study are available within the Article and Supplementary Information. Raw data files in other formats are available from the corresponding author upon reasonable request. Source data are provided with this paper.

Acknowledgements

We acknowledge primary support from the Department of Defense under grant W911NF2210115 (J.-W.K., M.J.A., E.A.R., L.M.S., H.L.C., A.U., Z.A.P.; compositional, optical, mechanical and thermal characterization, and materials and supplies). Partial support was provided by the Robert A. Welch Foundation under grants F-2007 (J.-W.K., A.U., Z.A.P.; synthesis) and F-2210 (A.J.A., G.E.S.; digital image correlation and rheology), National Science Foundation (NSF) Directorate for Engineering under grant 2229036 (A.G., W.E., M.A.C.; FEA and electronic device fabrication and testing), US Department of Energy, Office of Science, Basic Energy Sciences through the Center for Materials for Water and Energy Systems (M-WET), an Energy Frontier Research Center under award DE-SC0019272 (M.J.A., B.D.F.; nanoindentation characterization), NSF Graduate Research Fellowship under grant DGE-1610403 (M.J.A.) and Research Corporation for Science Advancement under award 28184 (Z.A.P.). The authors thank J. Rawlins at the University of Southern Mississippi for discussions on standardized aging conditions.

Author contributions

Conceptualization, J.-W.K., M.J.A., Z.A.P.; methodology, J.-W.K., M.J.A., E.A.R., L.M.S., H.L.C., A.U., A.G., W.E., A.J.A.; investigation, J.-W.K., M.J.A., E.A.R., L.M.S., H.L.C., A.U., A.G., W.E., A.J.A.; visualization, J.-W.K., M.J.A., E.A.R., Z.A.P.; funding acquisition, G.E.S., M.A.C., B.D.F., Z.A.P.; project administration, Z.A.P.; supervision, G.E.S., M.A.C., B.D.F., Z.A.P.; writing—original draft, J.-W.K., M.J.A., Z.A.P.; writing—review and editing, J.-W.K., M.J.A., E.A.R., L.M.S., H.L.C., A.U., A.G., W.E., A.J.A., G.E.S., M.A.C., B.D.F., Z.A.P.

Competing interests

Z.A.P., M.J.A. and J.-W.K. have filed an international patent (application no. PCT/US2024/035169) related to this work. The other authors declare no competing interests.

Additional information

Supplementary information The online version contains supplementary material available at https://doi.org/10.1038/s41563-025-02249-z.

Correspondence and requests for materials should be addressed to Zachariah A. Page.

Peer review information *Nature Materials* thanks Thomas Wallin and the other, anonymous, reviewer(s) for their contribution to the peer review of this work.